



Multiscale tomography of nanoporous carbon-supported noble metal catalyst layers

Simon Thiele^{a,*}, Tobias Fürstenthaupt^b, Dustin Banham^c, Tobias Hutzenlaub^a, Viola Birss^c, Christoph Ziegler^a, Roland Zengerle^a

^aLaboratory for MEMS Applications, IMTEK – Department of Microsystems Engineering, University of Freiburg, Georges-Koehler-Allee 103, 79110 Freiburg, Germany

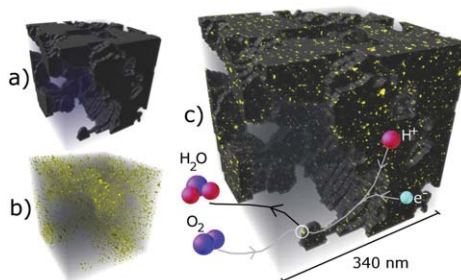
^bMicroscopy and Imaging Facility, University of Calgary, Health Sciences Centre B129, 3330 Hospital Drive NW, Calgary, AB T2N 1N4, Canada

^cDepartment of Chemistry, University of Calgary, 2500 University Drive NW, Calgary, AB T2N 1N4, Canada

HIGHLIGHTS

- ▶ A commercial PEMFC cathode catalyst layer is analyzed by multiscale tomography.
- ▶ We propose an approach to combine both tomography information in a single geometry.
- ▶ This enables analysis of limiting transport processes based on experimental data.

GRAPHICAL ABSTRACT



ARTICLE INFO

Article history:

Received 10 July 2012

Received in revised form

18 October 2012

Accepted 16 November 2012

Available online 1 December 2012

Keywords:

TEM tomography

FIB-SEM tomography

Polymer electrolyte membrane fuel cells

PEMFC

Catalyst

Nanoparticles

ABSTRACT

Noble metal catalysts are a scarce, non-renewable resource, and yet are required in a wide range of industrial applications, including in polymer electrolyte membrane fuel cells (PEMFCs). The effectiveness of PEMFCs depends not only on the size, active surface area, and distribution of the Pt catalyst nanoparticles, which affects reaction kinetics, but also on the porous structure of the carbon support, which affects mass transport. Unfortunately, the very different size scales – several nm for the Pt catalyst vs. several μm for the porosity features – cannot be characterized by a single method. Here, we present a novel approach for integrating information from both of these size scales to build a single geometrical model. Focused Ion Beam – Scanning Electron Microscope tomography (SEMt) was carried out on a commercial PEMFC cathode catalyst layer to characterize porosity, connectivity as well as pore-size and grain-size distribution. Transmission Electron Microscopy tomography (TEMt) was used to analyze volume and surface area distributions of nanometer sized platinum catalyst particles. Further, we propose an up-scaling approach to translate the information obtained from TEMt to SEMt. Knowledge of catalyst particle locations within the solid support matrix will be critical in enabling the analysis of limiting transport processes in PEMFC CCLs.

© 2012 Elsevier B.V. All rights reserved.

1. Introduction

Polymer electrolyte membrane fuel cells (PEMFCs) are considered to be an important part of the solution to the 21st century global energy challenge [1]. However, after decades of fundamental research, major challenges in the development of electrodes remain unsolved. In particular, the oxygen reduction reaction (ORR) and its

* Corresponding author. Tel.: +49 761 203 73247; fax: +49 761 203 73299.
E-mail address: simon.thiele@imtek.de (S. Thiele).

related transport processes in the Cathode Catalyst Layer (CCL) are generally considered to be one of the major causes of performance loss [2]. Not only are the kinetics of the ORR roughly six orders of magnitude slower than the hydrogen oxidation reaction at the anode [3], the production of H₂O at the cathode can also lead to flooding in the micron to nanometer sized pores in the CCL, thus inhibiting O₂ diffusion. Optimizing the PEMFC CCL is therefore a crucial area of research and requires a thorough understanding of the CCL structure, including the porosity, pore-size-distribution, ionomer distribution, catalyst loading, catalyst distribution and catalyst accessibility for the reactants.

As there is no analysis method which can be used to carry out *in situ* structural investigations at the nm scale, modeling the physical processes occurring at the nanoscale is therefore the only method currently available to improve the fundamental understanding of the CCL. Here electrons, protons and oxygen must come together at the catalytic Pt nanoparticle sites to enable the ORR. Therefore, the quantitative determination of the various transport processes in a CCL relies on detailed knowledge of the morphology of the transport media of the reactants [4]. Pt nanoparticles serve as catalysts for the ORR in a CCL and are a scarce, non-renewable resource, required in a wide range of industrial applications [5]. In PEMFCs, Pt nanoparticles (typically 3–6 nm in diameter) within the catalyst layers at both the anode and cathode are utilized to facilitate the desired redox reactions occurring at both electrodes [6]. Knowledge of the distribution and the precise location of the Pt nanoparticles in the CCL is therefore especially important to allow modeling of the performance of a PEMFC.

To date, there have been two main approaches to obtaining a three-dimensional CCL representation. One is a stochastic approach using assumptions about the material and the second involves a direct approach based on tomographic images. Stochastic reconstructions are three-dimensional structure models produced by utilizing microstructural descriptors [7]. From these, three-dimensional structure models can be produced by a mathematical optimization process [7–9].

The foundation of the direct approach is a three-dimensional image of the CCL. Different tomographic methods exist and each method has advantages and disadvantages as well as covering a specific feature size range [10]. The main advantage of this approach is that no further modeling assumptions must be made, thereby providing a realistic starting point for the CCL morphology. Design assumptions deduced from such a model are therefore more likely to result in improvements in the morphology and microstructure of the CCL.

In the past, Scanning Electron Microscopy (SEM) tomography (SEMt) analysis has been extensively used in material science, including for ceramic systems [11], cement analysis [12], solid oxide fuel cells [13], and very recently, also for PEMFC CCL studies [14]. This imaging method has an anisotropic resolution down to 10 nm in the cutting direction ('z-direction') and as low as 1 nm in the remaining directions ('x- and y-directions') [11]. SEMt is very well suited for the analysis of pore space with pores ranging from a few nm to a few hundred nm in size [15]. A number of publications have focused on PEMFC CCL SEMt within the last year [14–18]. A major drawback of this method, however, is that only pore and solid space can be distinguished [15]. This means that the solid phase cannot be further differentiated into its carbon, ionomer and Pt particle components.

Transmission Electron Microscopy tomography (TEMt) has been used for imaging and analysis of catalyst particles in the past [19,20]. Using this three-dimensional technique, detailed morphological information about the particles is then obtainable [19]. TEM tomography has also been used for the imaging of PEMFC CCLs [21]. Due to the high electron scattering of the noble metal catalyst component, PEMFC samples used for TEM tomography must be very

thin (e.g. 100 nm). While TEM, with its sub nm resolution, is excellent for characterizing the Pt nanoparticles in PEMFC CCLs, the typical pore-sizes in the solid support can be up to a few microns [4]. Therefore, a significant portion of the pore space cannot be evaluated by TEMt. While SEMt can differentiate the pore and solid spaces, TEMt provides the very much needed information about the catalyst particles, which is not accessible with SEMt, making these two techniques highly complementary to each another.

In the present work, we present an approach for capturing information from both of these size scales using only one geometric representation. The morphological information obtained from TEMt is combined with the information produced by SEMt and an up-scaling approach to translate the information obtained from TEMt to SEMt is proposed. It is important to note that, while our current work is focused on the application of this method to PEMFC CCLs, it has wider applicability, spanning many disciplines. Specifically, our approach will be of great value in all areas that utilize metal nanoparticles deposited in a porous matrix (e.g. electrodes for electrolysis, battery applications, automobile catalytic converters, etc.).

2. Experimental methods

A commercial Gore PRIMEA A510.1 M710.18 C510.4 PEMFC membrane electrode assembly (MEA) was used to carry out both TEMt and SEMt. The Pt loading (mass of Pt per unit surface area) was 0.1 mg cm⁻² at the anode and 0.4 mg cm⁻² at the cathode (Fig. 1). Spatial directions, indicated in the text and in Fig. 1, are maintained in all further discussions. For the SEMt, the surface of a cut is in the xy plane.

2.1. TEMt

All TEM work was performed using a Tecnai TF20 G2 FEG-TEM (FEI, Hillsboro, Oregon, USA), located in the Microscopy and Imaging Facility at the University of Calgary, with a Fischione 2040 Dual-Axis Tomography Holder (Fischione Instruments, Export, Pennsylvania, USA). The MEA was embedded in Epon-812 (EMS, Hatfield, Pennsylvania, USA) and approximately 200 nm thick sections were cut using a Leica Ultracut UCT (Leica Microsystems, Wetzlar, Germany).

The sections were placed on one side of a TEM Slot Grid (1 × 2 mm) that was covered with a ~40 nm thin continuous Formvar film (EMS). Colloidal Au particles (10 nm diameter, Cell Microscopy Center, University Medical Center Utrecht, Utrecht, The Netherlands) were

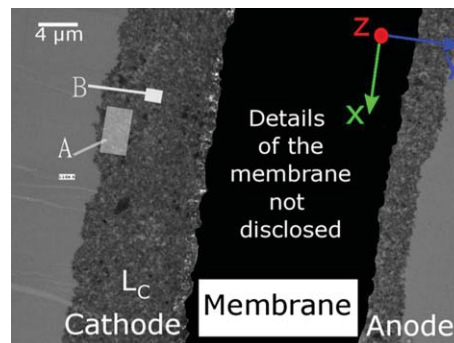


Fig. 1. Schematic of an ultra-microtome cut through the MEA. The cathode, ionomeric membrane separator, and anode are visible, but due to restrictions from the manufacturer, the membrane is blackened. The relative positions of the SEMt sample area (A) and TEMt sample area (B) are schematically indicated. The thickness of the cathode (L_c) is 11.4 ± 0.8 μm, as determined from this image. The x-, y- and z-directions are indicated and maintained in all further discussions.

placed on both sides of the section to serve as fiducial markers. Finally, a thin carbon coating was applied to both sides of the grid for mechanical stabilization and to reduce electrical charging in the microscope.

All TEM images were captured on a 1024×1024 pixel Gatan GIF 794 CCD (Gatan, Pleasanton, California, USA). Dual-axis TEMt was carried out by taking one image every degree over a range of between -65° and $+65^\circ$, using the program SerialEM [22]. The tomographic reconstruction was done by weighted back-projection with the IMOD software package, yielding a 3D image [23,24]. While Pt nanoparticles result in a good contrast, no contrast could be achieved using the present technique between carbon, the ionomer, and Epon-812. The 3D tomogram from the reconstruction was cut to $1024^\circ \times 980^\circ \times 274$ voxels. With a nominal resolution of 0.370 nm per pixel, this resulted in a tomogram $379 \text{ nm} \times 363 \text{ nm} \times 101 \text{ nm}$ in size. The original tomogram contained intrinsic noise that is manifested as a granularity on the pixel level (Fig. 2a).

These artifacts arise from two major sources. First, there is a loss of contrast from the embedding material. Second, the finite number of angles in the tomography procedure causes additional noise and optical artifacts. Both effects therefore resulted in artifacts after application of a threshold (Fig. 2b). Noise reduction was performed by applying an anisotropic diffusion filter implemented in Imagej (100 iterations, smoothing: 2, A1: 0.50, A2: 0.90, dt: 20.0 edge 5) (Fig. 2c) [25]. In this image, the 'adaptive 3D threshold' plug-in from Imagej was applied for segmentation (threshold: 95, mask diameter: 3 pixels, local weight: 5%). The resulting binary threshold image (Fig. 2d) showed a much more realistic distribution of Pt nanoparticles than a direct threshold image without the anisotropic diffusion step (Fig. 2b). Spherical colloidal Au particles located on the surface of the physical section were used as alignment markers for the tomographic reconstruction of the data. They are marked blue here and surrounded by a black circle (Fig. 2e).

They were manually removed by direct comparison of the original image with the resulting threshold image (Fig. 2e). Finally, single pixels were removed, as they are most likely noise from the segmentation process. This was done using the Matlab function 'bwareopen' and the six connected neighborhood option yielding the image series used for further analysis (Fig. 2f).

2.2. SEMt

For SEMt, an FIB (Focused Ion Beam) and an SEM are needed (Fig. 3a). Successively, the FIB ablates a slice of the sample, with the thickness of the cutting distance being ds . In the image collected by the SEM, information from both the surface and the cutting plane appears (Fig. 3b).

A Zeiss 'Neon 40EsB' was used for the FIB-SEM analysis. A $2.5 \times 2.5 \mu\text{m}^2$ Pt protection layer was deposited on the surface of the cathode catalyst layer using a 30 kV acceleration voltage at a current of 5 pA for 200 s (Fig. 3b). Fiducial marks were inscribed with the FIB to facilitate the alignment process at 30 kV acceleration voltage and 50 pA current. A cuboid of $6 \mu\text{m} \times 4 \mu\text{m} \times 10 \mu\text{m}$ (x -, y - and z -directions) was exposed by FIB milling at 30 kV acceleration voltage and 500 pA current. Fine polishing by FIB was performed at 30 kV acceleration voltage and a current of 50 pA. A series of 120 images, with a cutting distance of 13.6 nm in z -direction and an x - and y resolution of 2.5 nm, was collected, using the following parameters: FIB: 30 kV acceleration voltage and 50 pA, SEM: 2 kV acceleration voltage.

The complete experimental reconstruction procedure for SEMt followed the approach described in [15]. As described there, the segmentation was done semi-automatically by first using a threshold and subsequently performing a manual correction of the images by using the software gimp. Algorithms for calculating the pore-size-distribution or the grain-size distribution need an integer

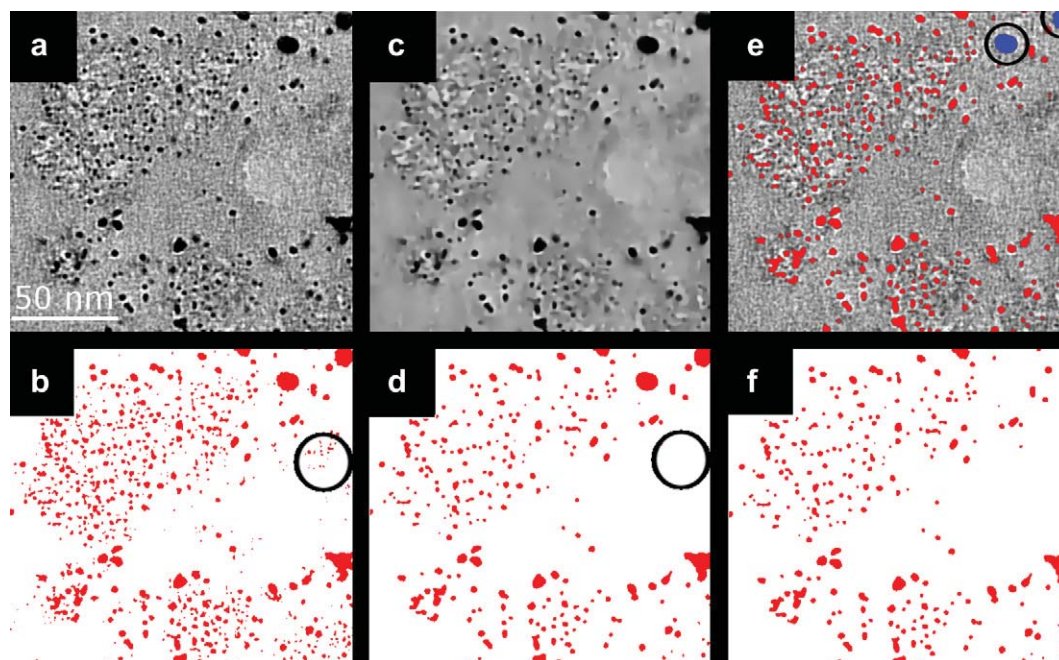


Fig. 2. The steps associated with the TEM tomography segmentation process are illustrated here. (a) A 700×700 pixels sub-area from the original TEM tomogram, with Pt particles shown in black. (b) A threshold image from the original tomogram, with noise and segmentation artifacts being visible. Within the black circle, artifacts (granularity on the pixel level) from the reconstruction are shown. (c) An anisotropic diffusion filtered version of (a), with much less noise seen, while the edges of the Pt particles remain sharp. (d) A threshold image from the 'adaptive 3D threshold plug-in', with the segmentation artifacts seen in (b) no longer present. (e) is the superposition of (c) and (d). Two gold fiducial markers that are artificially introduced during sample preparation to help the tomographic reconstruction are marked in blue and encircled. These markers were manually removed for the final segmentation. (f) Final segmentation without marker particles. (For interpretation of the references to colour in this figure legend, the reader is referred to the web version of this article.)

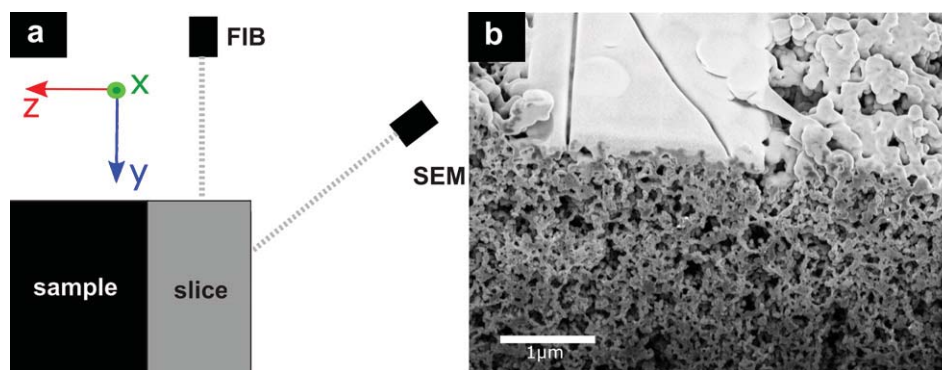


Fig. 3. (a) Sketch of the experimental set-up for a SEMt reconstruction. xy planes are cut in the z -direction with the image acquisition at an angle of 54° between FIB and SEM. (b) One image of the SEMt image series. The upper part of the image shows the surface of the sample with the Pt protection layer containing a V-shaped fiducial mark. In the lower part of the image, the inner porous structure of the CCL can be seen, showing that FIB-SEM can only discern the pores and solid phases and that the individual Pt, carbon, and ionomer phases cannot be resolved.

number ratio between the resolution in the z -direction and the xy -direction. Therefore, the resolution of the xy -direction was rescaled from $2.5 \text{ nm} \times 2.5 \text{ nm}$ to $3.4 \text{ nm} \times 3.4 \text{ nm}$ by linear interpolation. This resulted in a voxel size of $3.4 \text{ nm} \times 3.4 \text{ nm} \times 13.6 \text{ nm}$. The geometry was cropped to a size of $1.6 \mu\text{m} \times 1.6 \mu\text{m} \times 1.6 \mu\text{m}$ or $480 \times 480 \times 120$ voxels. To facilitate further computer-aided analysis, the inhomogeneous voxels, with an edge length ratio of $1 \times 1 \times 4$, were replaced by four identical voxels of a ratio of $1 \times 1 \times 1$. Finally, isolated areas too small to have any physical meaning, were erased from both the solid and porous phases. This was performed by utilizing the `bwareopen` function, thus removing 2D areas smaller than 10 pixels (115.6 nm^2 or 12.1 nm diameter). As a result, a porous 3D matrix was available for further investigation.

3. Results and discussion

3.1. SEMt

Only the pores and total solid phase could be differentiated from each other in the SEMt images. Further differentiation of the solid phase into its carbon, ionomer, and Pt components was not possible. A connectivity analysis of the pore space was performed, as described in [15]. The porosity of the porous 3D matrix was 58% (Fig. 4), with 99.8% of the solid area being inter-connected. The remaining 0.2% can be considered as artifacts. Also 99.9% of the pore area is connected. Only the connected areas were used for further calculations. To determine if the geometry is representative, it was subdivided into eight, four and two partitions along the main axes (x , y , z). For each partitioning, all possible combinations were tested. For example, a partitioning into four parts can be achieved in three different ways, i.e., by dividing along x and y , along x and z or along y and z . An individual porosity for all sub-volumes using every possible partitioning was calculated and the standard deviations between the sub-volumes were determined.

This was done for a partitioning into eight, four and two parts and yielded porosity standard deviations of 4%, 3% and 1.4%. This indicates that the sample shown in Fig. 4 closely represents the characteristics of the whole CCL sublayer. The pore-size-distribution (PSD) and the grain-size-distribution (GSD) were also calculated to characterize the porous and solid phases, respectively. The GSD is calculated similarly to a PSD but using the solid phase. The word 'grain' refers here to the local dimensions in the solid part and comes from a particle analysis background. These calculations were performed following the approach described in [15] and [26]. The PSD shows a rather broad distribution (Fig. 5) with pore diameters between 7 and 275 nm, while the GSD showed a clear

peak at 65 nm diameter. The solid phase contained diameters between 7 and 210 nm.

In relation to the PSD, the GSD is rather narrow, with 75% of the grain diameters being between 31 and 102 nm in size and 58% of the diameters being between 44 and 92 nm (Fig. 5). The peak at 65 nm indicates that, in the catalyst layer manufacturing process, carbon particles in this size range are used by the manufacturer or alternatively that agglomerates of this size are preferentially formed during the manufacturing process. This result can easily be used in future stochastic modeling of PEMFC CCLs utilizing PSD and GSD as an input parameter. However, for a more detailed analysis of reactant transport to reaction centers, it is important to know where the Pt particles are located. With a typical Pt particle size range of 3–6 nm, and a SEMt resolution of 13.6 nm in the z - and 3.4 nm in the x - and y -directions, resolving the Pt nanoparticles is obviously not possible using SEMt. Fortunately, it is possible to achieve this goal using TEMt as is shown in the next section.

3.2. TEMt

The first important result from the TEMt analysis is that the Pt nanoparticles can be imaged, as described in Section 2. While Pt

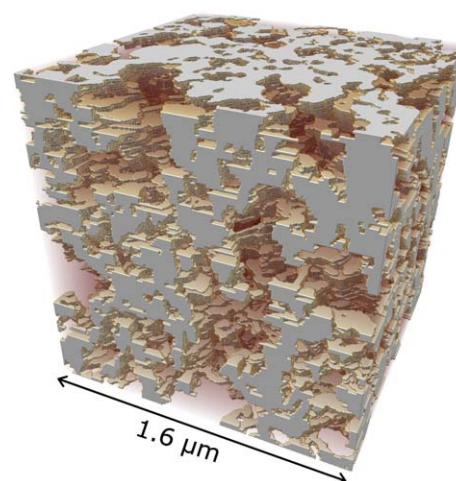


Fig. 4. A 3D representation of the reconstructed SEMt dataset. A volume with dimensions of $1.6 \mu\text{m} \times 1.6 \mu\text{m} \times 1.6 \mu\text{m}$ is shown. The solid part of the sample is depicted in grey, while pores are 99% transparent. For a better visualization, the pore space is depicted with a 1% opacity in red. The porous material shows a porosity of 58% and a connectivity of the solid parts of more than 99.8%. (For interpretation of the references to colour in this figure legend, the reader is referred to the web version of this article.)

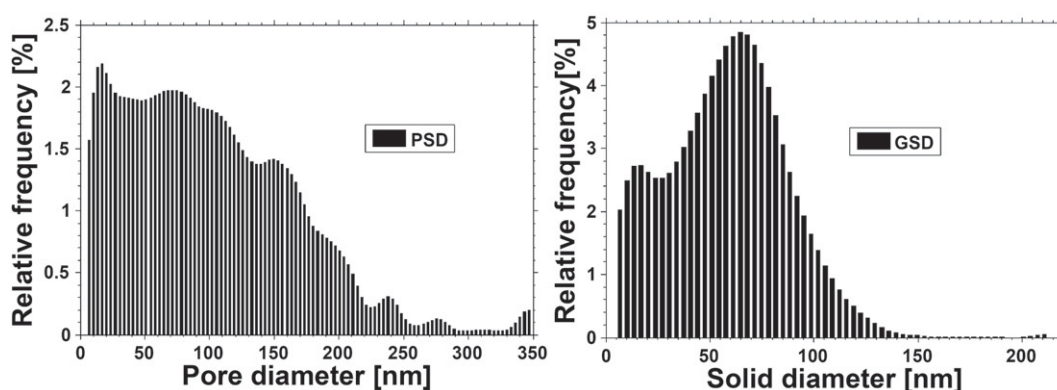


Fig. 5. The pore-size-distribution (PSD) and the grain-size-distribution (GSD) calculated from the SEMt dataset. In the PSD, all pore diameters range between 7 and 350 nm. In the GSD, grain-size diameters between 7 and 210 nm were found with a pronounced peak at 65 nm. The PSD and GSD are important results that can serve as input for stochastic modeling in the future.

nanoparticles have good contrast, no contrast could be achieved between the carbon particles, the Nafion ionomer, and the Epon-812 (a polymer) filling the pores (Fig. 6). This means that no porosity information can be obtained from the TEMt analysis.

A careful investigation of the TEMt and the TEM images revealed that the Pt nanoparticles are randomly distributed throughout the solid phase of the sample. This important observation is used in Section 3.3 to motivate the random inscription of Pt particles into the solid phase. An overall number of 13,862 Pt nanoparticles were found in the sample (Fig. 6). There are areas with rather high amounts of Pt and areas with only a few particles. The sample contains an overall Pt volume of $3.71 \times 10^{-22} \text{ m}^3$ corresponding to a 2.7 vol % Pt.

For each Pt particle, its volume was then determined and a corresponding diameter calculated, assuming a spherical particle shape in order to make this distribution comparable to experimentally determined particle diameter distributions. The biggest particle has a diameter of 32 nm. 99.9% of the particles have diameters between 0.58 nm and 15 nm. For a better visualization, only this range of particles is shown (Fig. 7). Particles smaller than 0.58 nm in diameter cannot be resolved. It has, however, been shown that the most active Pt particles are in the range of 2–5 nm [27]. Therefore, the tomographic approach presented in this work can be considered as precise enough to image the catalytically important particle size range. The mean diameter of this distribution is $2.8 \pm 1.5 \text{ nm}$. The peak between 1.5 nm and 3 nm shows that there are relatively small particles in the sample.

According to the method shown in [28], the total surface area of the Pt particles was determined to be $6.6 \times 10^{-13} \text{ m}^2$. The biggest single particle has a volume of $1.75 \times 10^{-23} \text{ m}^3$ and a surface area of $2.23 \times 10^{-14} \text{ m}^2$. A total of 99.7% of the particles have a volume of

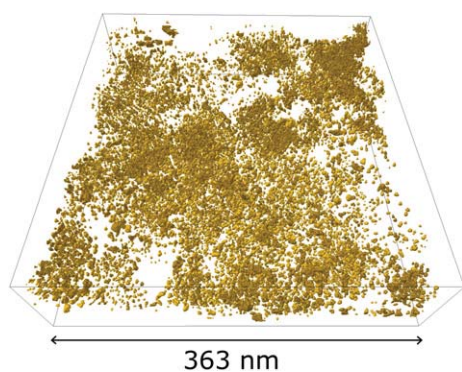


Fig. 6. The whole TEMt sample of $379 \text{ nm} \times 363 \text{ nm} \times 101 \text{ nm}$.

less than $5 \times 10^{-25} \text{ m}^3$. For better visualization of the particle distribution, only the range between 0 and $5 \times 10^{-25} \text{ m}^3$ is shown in a volume–surface area scatterplot (Fig. 8). A comparison between the particle distribution (blue) and perfect spheres (black) clearly indicates that the particles are mostly non-spherical.

This is in accordance with previous TEMt analyses of carbon-supported Pt, where it was shown that the Pt particles had a non-spherical shape [29]. However, the Pt particle shapes found in our 3D TEMt images are different from the spherical shapes seen in 2D TEM images (e.g. [27]). It should be noted that there are different effects in TEMt that can lead to reconstruction artifacts, thus hindering the determination of the true particle structure. These effects include the ‘missing wedge’ effect, which occurs due to the mechanical and sample dependent limitations on the upper tilt angle that is achievable as well as the influence of neighboring particles [30]. The missing wedge effect can be diminished by dual-axis tomography, which has been done here on the present sample, but the influence of neighboring particles on the particle shape cannot be excluded in a sample with high particle density areas present (Fig. 6). Another source of artifacts can be introduced by the support matrix and is known as the ‘top-bottom effect’ [31]. Again, for a supported material, this effect is difficult to avoid. All of the effects mentioned above should be excluded in future studies, but this is beyond the scope of the present paper.

Clearly, TEMt allows access to important morphological information, such as the surface area and/or volume of a single Pt particle. This is of great importance in the determination of Pt utilization within the CCL, allowing comparisons to be made between the TEMt-estimated Pt surface area and the electrochemically

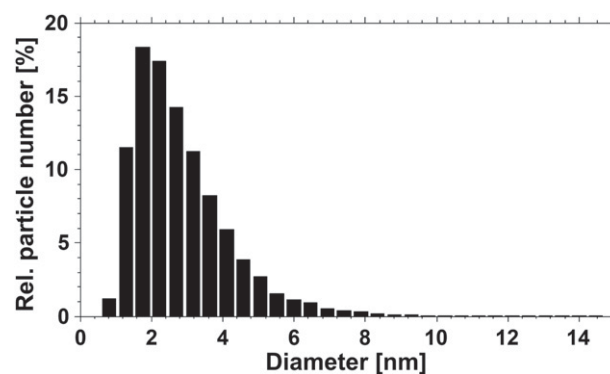


Fig. 7. The relative number of Pt particles as a function of their diameter. A clear peak can be seen between Pt particle sizes of 1.5 nm and 3 nm.

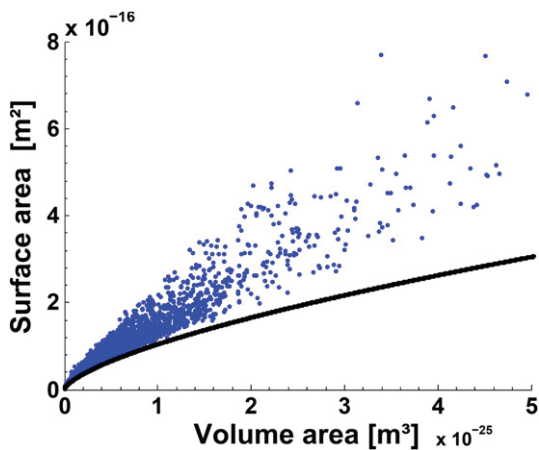


Fig. 8. Shows a scatterplot of the single particle surface area as a function of particle volume (blue). The black line corresponds to perfect spheres and naturally depicts the minimum of the surface to volume ratio. 98.7% of the particles have a volume below $2 \times 10^{-25} \text{ m}^3$ and 96.0% have a volume below $1 \times 10^{-25} \text{ m}^3$. (For interpretation of the references to colour in this figure legend, the reader is referred to the web version of this article.)

determined Pt surface area from hydrogen underpotential deposition measurements [32]. It is therefore very evident that SEMt and TEMt are highly complementary methods, each giving essential, but unique, information about the solid phases in the PEMFC CCL. To use both information sources at the same time, it is now necessary to combine these two tomographic datasets.

3.3. Integration of Pt distribution from TEMt into SEMt geometry

In the following section, we introduce a method that transfers morphology information generated by TEMt, with a resolution of 0.37 nm per pixel, to the higher scale of SEMt, having a resolution of 3.4 nm per pixel. This will be called ‘up-scaling’ and it makes information describing Pt particle volume and surface area accessible at this higher magnification. The up-scaling method involves the following steps:

1. The total Pt volume in the SEMt representation (V_{PtSEMt}) is calculated by using manufacturer information. This is necessary, because within the small TEMt sample volume, the porosity is not known (see Section 3.2).
2. The number of times that the TEMt Pt particle distributions must be inscribed into the SEMt geometry to achieve the desired loading given from the manufacturer is calculated.
3. Inscribing the volume and surface values into the solid part of the SEMt representation results in two 3D matrixes, with one representing the Pt volume information and the other representing the Pt surface information.

In the following discussion, we give a detailed insight into all three of the up-scaling process steps (1)–(3).

- (1) According to the manufacturer, the PEMFC CCL has a Pt loading of 0.4 mg cm^{-2} . The thickness of the sample was measured at ten different locations using ultra-microtome cuts from the sample (Fig. 1) and determined to be $11.4 \pm 0.8 \mu\text{m}$. With this information and the value for the Pt density of 21.45 g cm^{-3} , the Pt vol% in the sample is found to be 1.6 vol% and the total Pt volume (V_{PtSEMt}) is $6.95 \times 10^{-20} \text{ m}^3$.
- (2) In the TEMt representation, we found a relative Pt volume fraction of 2.7 vol%, which is higher than the 1.6 vol% calculated from the manufacturer information. This naturally results from

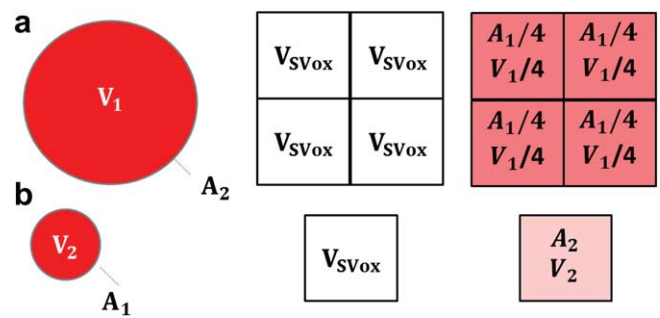


Fig. 9. There are two cases that can naturally appear when distributing particle volumes into a limited volume: (a) the particle volume can be larger than a single voxel. In this case, the particle volume must be distributed over more than one voxel. (b) The particle volume can be smaller than a single voxel, so that the single particle fits into a single SEMt voxel.

the fact that, for the TEMt representation, a volume with a large amount of solid was chosen so that a good statistical estimate for the Pt particle distribution could be made. Therefore, to achieve a representative Pt loading, the Pt particles from the TEMt geometry had to be distributed N times into the SEMt geometry, using $V_{\text{PtTEMt}} = 3.75 \times 10^{-22}$ yields:

$$N = \frac{V_{\text{PtSEMt}}}{V_{\text{PtTEMt}}} = 185.2 \approx 185 \quad (1)$$

- (3) For inscription of the Pt particles into the SEMt geometry using a statistical process, some rules have to be defined. Due to the random distribution of Pt throughout the solid phase (Section 3.2), the locations in the solid matrix are chosen randomly without any preferential areas. From Fig. 7, we know that there are several Pt particles larger than a SEMt voxel (3.4 nm). Pt particles having volumes smaller than one SEMt voxel are thus placed into one single SEMt voxel. Even more than one Pt particle can be placed into the same SEMt voxel as long as the total Pt volume does not exceed the SEMt voxel volume. For Pt particles larger than one SEMt voxel, the minimum number of neighboring SEMt voxels needed to contain the complete particle volume is determined. In that case, the Pt particle volume is equally distributed over all voxels representing the same particle (Fig. 9). As a further rule, no Pt particles are inscribed if the SEMt voxels represent the porous phase (Fig. 10a).

Two geometries are thus generated, representing first the Pt volume distribution (Fig. 10b) and second the Pt surface distribution (Fig. 10c). Both distributions yield different information, as the Pt particles are not spherical. The volume of the particle is placed into one 3-dimensional matrix, whereas the surface area is inscribed into another three-dimensional matrix. The surface area information from each Pt particle is inscribed at the same location in the solid as the corresponding volume information. For Pt particles larger than one voxel, the Pt surface information is only inscribed at those voxels that represent the external surface of the inscribed particles (Fig. 10c) and not to those representing the inside of a Pt particle. In this case, the SEMt shape of particles larger than a voxel is modeled as spherical for reasons of simplicity. This entire approach was fully implemented into Matlab.

3.4. Implications from the up-scaled geometry for future PEMFC CCL models

At the Pt particle locations, oxygen, protons and electrons have to come together for the reaction to occur. Oxygen diffuses through the pores as long as they are not blocked by water. In this case O_2

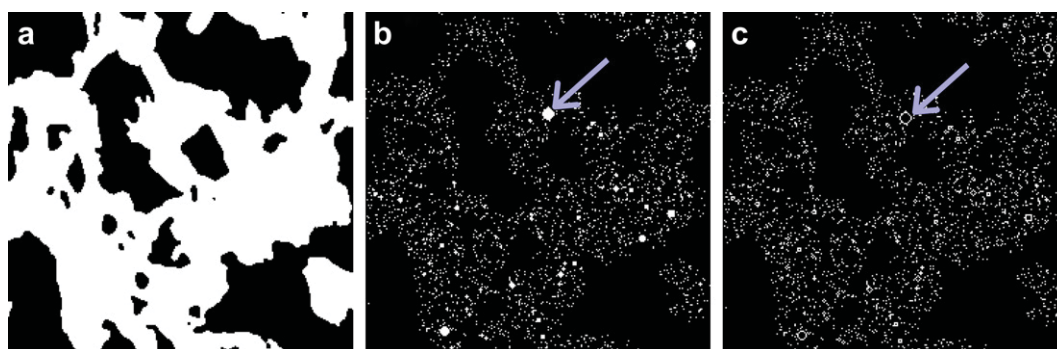


Fig. 10. (a) A $850 \text{ nm} \times 850 \text{ nm}$ cut from the 3D representation of the SEMt sample, with the solids shown in white and the porous area in black. (b) The same cut in the up-scaled Pt volume representation. Larger particles have a spherical shape, as indicated with an arrow. (c) The Pt surface representation with all pixels containing surface information greater than zero shown in white. For Pt particles larger than one voxel, the Pt surface information is only inscribed at those voxels that represent the particle external surface and not to those representing the inside of a Pt particle (see arrow). This makes sense for the simulation of transport processes, as reactions will take place only at the Pt particle surface and not inside the Pt particle.

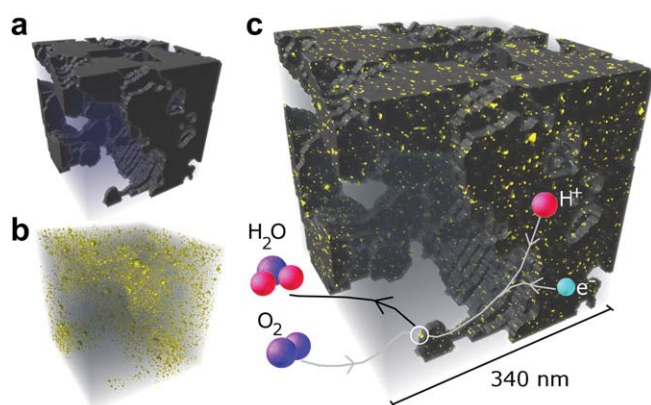


Fig. 11. (a) A cube of 340 nm side length of the SEMt reconstruction. (b) The reconstructed Pt volume information in the same spatial area as the SEMt reconstruction. (c) The superposition of (a) and (b) and visualizes the location of Pt catalyst particle volume and surface information within the porous carbon matrix. At the Pt nanoparticle locations, oxygen, protons, and electrons have to come together for the ORR to occur, as is schematically depicted. Oxygen diffuses from the outside through the pores, provided they are not blocked by water. Protons are transported by the ionomer contained in the solid as well as the water contained in the pores. Electrons are transported by the carbon contained in the solid. Finally, water vapor must be transported out of the CCL through the pores.

diffusion still occurs, but is greatly impeded. Protons are transported by the ionomer contained in the solid as well as the liquid water contained in the pores. Electrons are transported by the carbon contained in the solid. Water vapor is produced by the reaction and must be transported out of the CCL through the pores. Knowing the locations of the active centers enables modeling of the transport limitations that occur (Fig. 11) and subsequently the optimization of the CCL. By the combined use of SEMt (Fig. 11a) and up-scaled TEMt (Fig. 11b) a microstructure model of Pt catalyst particles embedded in a porous matrix is made available (Fig. 11c). On this way knowledge on the positions of active centers as well as their morphologic properties such as single particle volume and surface are given. This can be seen as the first necessary step to modeling the whole reactant transport in a realistic geometry in future work.

4. Conclusions

Here, for the first time, TEMt and SEMt information was combined, enabling the visualization of the location and morphological properties of the Pt nanoparticles embedded in the porous

carbon matrix at very different length scales from several nanometers up to micrometers. This information is crucial for modeling the limiting transport processes in the high current density regime of a PEMFC CCL.

SEMt analysis revealed a preferential size in the GSD of about 65 nm and the pore-size-distribution (PSD) showed highly porous material characteristics with 58% porosity and pores ranging from 7 nm to 350 nm . TEMt analysis revealed an average Pt particle size of $2.8 \pm 1.45 \text{ nm}$, and non-spherical shapes.

A relatively simple approach was applied for integrating TEMt information into SEMt, based on the Pt loading (obtained from the manufacturer) and the single particle surface area and volume distribution obtained from TEMt. The combined information of SEMt and TEMt simultaneously yields knowledge of both the available reaction pathways, and the distribution and number of reaction Pt sites. Knowledge of the accessibility of reaction centers to the reactants (oxygen and protons) will enhance the current understanding of voltage losses at high current densities in a PEMFC CCL. The advantage of this approach vs. stochastic methods is that the starting point for all of the calculations is based on tomographic data from real commercial available materials.

Acknowledgements

This work is part of the project PEM-Ca-D (Grant No. 03SF0360D) and is funded by the German Ministry of Education and Research (BMBF). We also gratefully acknowledge the Natural Sciences and Engineering Research Council of Canada (NSERC) and Alberta Innovates-Technology Futures (AITF) for the support of this work. This work was supported by an equipment and infrastructure grant from the Canadian Foundation for Innovation (CFI) and the Alberta Science and Research Authority.

References

- [1] Y. Wang, K.S. Chen, J. Mishler, S.C. Cho, X.C. Adroher, *Applied Energy* 88 (4) (2011) 981–1007.
- [2] D. Gerteisen, T. Heilmann, C. Ziegler, *Journal of Power Sources* 187 (1) (2009) 165–181.
- [3] H.A. Gasteiger, S.G. Yan, *Journal of Power Sources* 127 (1) (2004) 162–171.
- [4] M. Eikerling, *Journal of Electrochemical Society* 153 (2006) E58.
- [5] R.B. Gordon, M. Bertram, T.E. Graedel, *Proceedings of National Academy of Sciences USA* 103 (5) (2006) 1209.
- [6] S.H. Joo, K. Kwon, D.J. You, C. Pak, H. Chang, J.M. Kim, *Electrochimica Acta* 54 (24) (2009) 5746–5753.
- [7] S. Torquato, *Annual Review of Materials Research* 32 (1) (2002) 77–111.
- [8] P. Levitz, *Advances in Colloid and Interface Science* 76 (1998) 71–106.
- [9] P.P. Mukherjee, C.Y. Wang, *Journal of Electrochemical Society* 154(2007) B1121.

- [10] G. Möbus, B.J. Inkson, *Materials Today* 10 (12) (2007) 18–25.
- [11] L. Holzer, F. Indutnyi, P.H. Gasser, B. Munch, M. Wegmann, *Journal of Microscopy* 216 (1) (2004) 84.
- [12] L. Holzer, B. Muench, M. Wegmann, P. Gasser, R.J. Flatt, *Journal of American Ceramic Society* 89 (8) (2006) 2577–2585.
- [13] J.R. Wilson, W. Kobsiriphat, R. Mendoza, H.Y. Chen, J.M. Hiller, D.J. Miller, K. Thornton, P.W. Voorhees, S.B. Adler, S.A. Barnett, *Nature Materials* 5 (7) (2006) 541–544.
- [14] C. Ziegler, S. Thiele, R. Zengerle, *Journal of Power Sources* 196 (4) (2011) 2094–2097.
- [15] S. Thiele, R. Zengerle, C. Ziegler, *Nano Research* 4 (9) (2011) 849–860.
- [16] J. Balach, F. Miguel, F. Soldera, D.F. Acevedo, F. Mücklich, C.A. Barbero, *Journal of Microscopy* 246 (3) (2012) 274–278.
- [17] A. Çeçen, E.A. Wargo, A.C. Hanna, D.M. Turner, S.R. Kalidindi, E.C. Kumbur, *Journal of Electrochemical Society* 159 (2012) B299.
- [18] H. Schulenburg, B. Schwanitz, N. Linse, G.G. Scherer, A. Wokaun, J. Krbanjevic, R. Grothausmann, I. Manke, *Journal of Physical Chemistry C* 115 (29) (2011) 14,236–14,243.
- [19] T. Ito, U. Matsuwaki, Y. Otsuka, G. Katagiri, M. Kato, K. Matsubara, Y. Aoyama, H. Jinnai, *Direct Three-dimensional Visualization and Morphological Analysis of Pt Particles Supported on Carbon by Transmission Electron Microtomography*, Wiley Online Library, 2010.
- [20] A.J. Koster, U. Ziese, A.J. Verkleij, A.H. Janssen, K.P. De Jong, *Journal of Physical Chemistry B* 104 (40) (2000) 9368–9370.
- [21] H. Uchida, J.M. Song, S. Suzuki, E. Nakazawa, N. Baba, M. Watanabe, *Journal of Physical Chemistry B* 110 (27) (2006) 13,319–13,321.
- [22] D.N. Mastronarde, *Journal of Structural Biology* 152 (1) (2005) 36–51.
- [23] J.R. Kremer, D.N. Mastronarde, J.R. McIntosh, *Journal of Structural Biology* 116 (1) (1996) 71–76.
- [24] D.N. Mastronarde, *Journal of Structural Biology* 120 (3) (1997) 343–352.
- [25] D. Tschumperle, R. Deriche, *IEEE Transactions on Pattern Analysis and Machine Intelligence* (2005) 506–517.
- [26] T. Hutzenlaub, S. Thiele, R. Zengerle, C. Ziegler, *Electrochemical and Solid State Letters* 15 (2012) A33.
- [27] C.V. Rao, B. Viswanathan, *Journal of Physical Chemistry C* 114 (18) (2010) 8661–8667.
- [28] J. Lindblad, *Image and Vision Computing* 23 (2) (2005) 111–122.
- [29] L.C. Gontard, R.E. Dunin Borkowski, D. Ozkaya, *Journal of Microscopy* 232 (2) (2008) 248–259.
- [30] P.A. Midgley, R.E. Dunin Borkowski, *Nature Materials* 8 (4) (2009) 271–280.
- [31] C. Yang, H.B. Zhang, J.J. Li, A. Takaoka, *Journal of Electron Microscopy* 54 (4) (2005) 367–371.
- [32] N. Markovic, H. Gasteiger, P.N. Ross, *Journal of Electrochemical Society* 144 (5) (1997) 1591–1597.